nature research

https://doi.org/10.1038/s41566-020-00729-z

Supplementary information

Optical analogue of Dresselhaus spin–orbit interaction in photonic graphene

In the format provided by the authors and unedited

Supplementary material for "Optical analogue of Dresselhaus spin-orbit interaction in photonic graphene"

C. E. Whittaker,[1] T. Dowling,[1] A. V. Nalitov,[2,3,4] A. V. Yulin,[4] B. Royall,[1]
E. Clarke,[5] M. S. Skolnick,[1,4] I. A. Shelykh,[3,4] and D. N. Krizhanovskii[1,4]

[1]*Department of Physics and Astronomy, University of Sheffield, Sheffield S3 7RH, United Kingdom*
[2]*Faculty of Science and Engineering, University of Wolverhampton, Wulfruna Street, Wolverhampton WV1 1LY, UK*
[3]*Science Institute, University of Iceland, Dunhagi-3, IS-107 Reykjavik, Iceland*
[4]*ITMO University, St. Petersburg 197101, Russia*
[5]*EPSRC National Epitaxy Facility, University of Sheffield, Sheffield S1 3JD, United Kingdom*

Contents

I. CALCULATED SPIN PATTERNS

The spin patterns observed in the experiment are determined by the Dresselhaus-type structure of the part of the Hamiltonian describing TE-TM splitting in the system. Before presenting the results of full numerical analysis, let us show this explicitly.

The 4x4 Hamiltonian (1) of the main text of the article can be represented in the following block form, with 2x2 non zero blocks standing off diagonal:

$$H^D = \begin{pmatrix} 0 & \hbar v_F \tau_z q_x - \Delta s_x - i(\hbar v_F q_y + \Delta \tau_z s_y) \\ \hbar v_F \tau_z q_x - \Delta s_x - i(\hbar v_F q_y + \Delta \tau_z s_y) & 0 \end{pmatrix}. \tag{S1}$$

By use of the unitary transformation, corresponding to the diagonalization in sublattice pseudospin, but not in the polarization space, i.e. going to the representation of upper and lower Dirac cones, one can transform this Hamiltonian into block diagonal form:

$$H^D = \begin{pmatrix} +H^{(2)} & 0 \\ 0 & -H^{(2)} \end{pmatrix} \tag{S2}$$

where the upper block corresponds to a pair of upper Dirac cones with two orthogonal polarizations, and the lower block to a pair of lower Dirac cones, and 2x2 blocks $H^{(2)}$ are:

$$H^{(2)} = \sqrt{\hbar^2 v_F^2 q^2 + 2\hbar v_F \tau_z \Delta (q_y s_y - q_x s_x) + 2\Delta^2 (1 - s_z)}. \tag{S3}$$

In the limit $\hbar v_F q \gg \Delta$, corresponding to the asymptotically linear dispersion branches, one can use Taylor decomposition in the above equation to obtain:

$$H^{(2)} = \hbar v_F q + \tau_z \Delta \frac{q_y s_y - q_x s_x}{q} \tag{S4}$$

The two terms in the above representation may be interpreted as the standard linear Dirac part $\hbar v_F q$, supplemented with the effective spin-orbit coupling term $\pm\Delta(q_y s_y - q_x s_x)/q$, where the $\pm$ sign is defined by the product of the valley index τ_z and the index of the Dirac cone (plus for upper, minus for lower cone). This effective spin-orbit coupling fully reproduces the angular dependence of the Dresselhaus Hamiltonian for 2D electron systems, while being independent on the momentum absolute value q, in contrast to the linear momentum dependence of the Dresselhaus term.

Now, let us describe the procedure which can be used to numerically reproduce the spin patterns generated in the optical spin Hall effect (OSHE). In the case of quasi-resonant pumping of the Dirac points the polariton wavefunction obeys the generalized Schrödinger equation:

$$i\hbar\dot{\Psi} = \left[H^D - i\hbar\Gamma\right]\Psi + P_0 e^{-q^2L^2/4} e^{-i\omega t}, \tag{S5}$$

where H^D is the effective Hamiltonian close to the Dirac points (see Eq. (1) in Methods section of main text) and Γ is the polariton linewidth. The second term on the right hand side describes in-phase excitation of both sublattices by a pump of size L with energy ω and amplitude and polarization given by P_0. $P_0 = (1,1,1,1)^T$ for horizontal polarization and $P_0 = (1,-1,1,-1)^T$ for vertical polarization. q is the wave vector deviation from the Dirac point. The stationary solution then reads

$$\Psi_0 = P_0 e^{-q^2L^2/4}\left[\hbar(\omega + i\Gamma) - H^D\right]^{-1}. \tag{S6}$$

The corresponding real space wavefunction, which is what we observe in experiment, is then obtained using an inverse Fourier transform. In Figs. S1 and S2 we plot the calculated real space spin distribution corresponding to the excitation conditions of Figs. 3 and 4 of the main text.

We note that the same procedure can be used for H^Γ (i.e. excitation near the Γ point) to produce four-fold spin patterns as observed in the conventional OSHE[1].

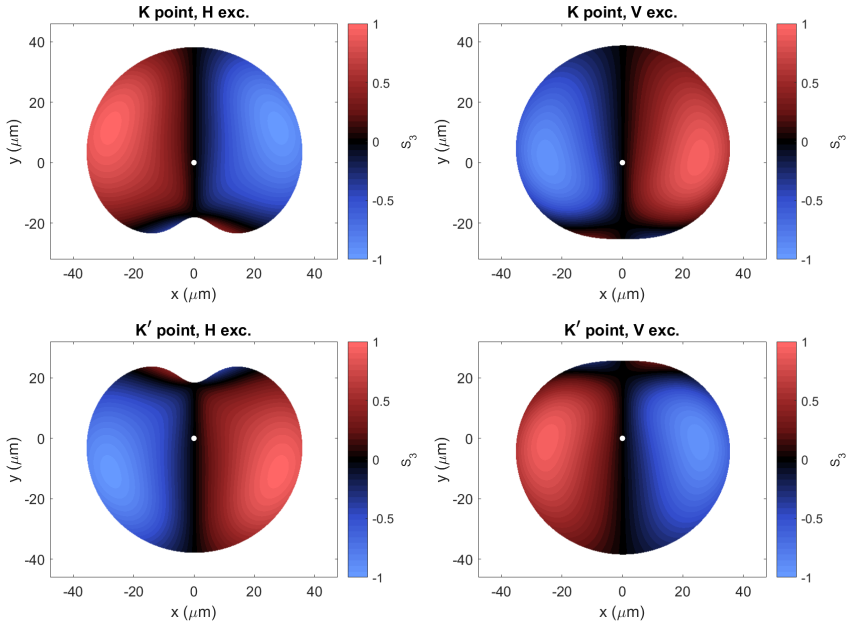

FIG. S1: Calculated spin patterns for quasi-resonant excitation of the s-band Dirac points. The following parameters, based on experimental values, are used: $J = 0.12$ meV, $\delta J = 0.018$ meV, $\omega = 0.03$ meV, $\Gamma = 0.04$ meV and $L = 15$ μm. The images are cropped where the intensity drops to 1% of the maximum value, which is the approximate noise level in experiment. The white marker shows the position of the excitation spot.

Note, that in the simulated real space spin patterns there are weak traces of a four-leaf pattern visible in the peripheral area where the field intensity drops down to 1% of the peak maxima (weakly visible in the experimental Fig. 3 also). Generally, the spin patterns in the OSHE can be viewed as the interference between polariton modes

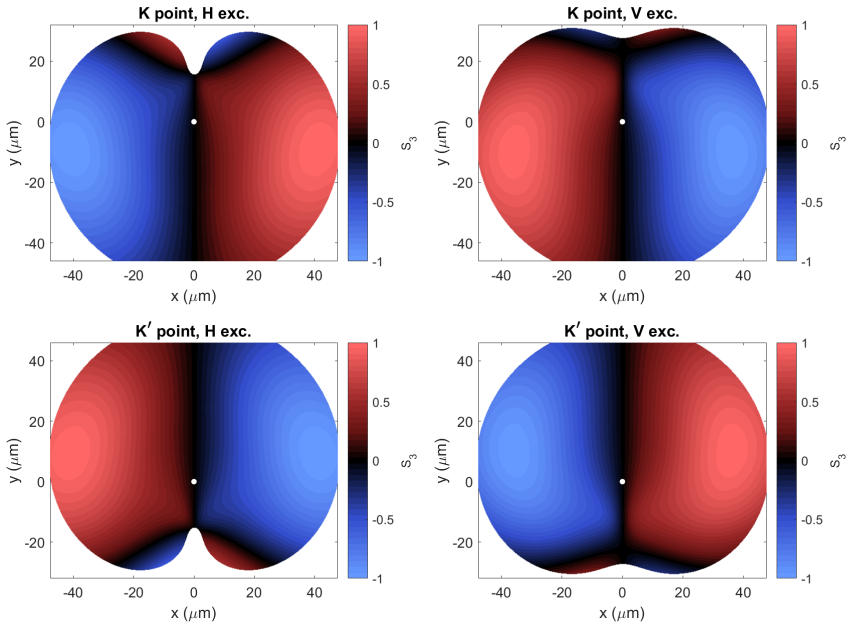

FIG. S2: Calculated spin patterns for quasi-resonant excitation of the p-band Dirac points. The tunnelling energies are based on experimental parameters corresponding to $J = -0.6$ meV, $\delta J = 0.05$ meV, with additional parameters $\omega = 0.03$ meV, $\Gamma = 0.06$ meV and $L = 15$ μm. The images are cropped where the intensity drops to 1% of the maximum value, which is the approximate noise level in experiment. The white marker shows the position of the excitation spot.

of different linear polarization, which are resonantly excited at various k-vectors by the CW pump focused into a finite spot. In a realistic scenario not all modes are excited equally however, since the excitation efficiency at a particular k close to the Dirac point depends on a combination of the pump frequency, polariton linewidth (losses Γ), pump polarization and valley index. Slightly different weights of the resonantly excited interfering polariton branches can make the interference pattern more complicated than an ideal two-leaf structure. In simulations the purity of the two-leaf structure can be increased significantly by the appropriate adjustment of the excitation parameters, for example, by increase in polariton losses or the frequency of the pump. A detailed analysis of this effect is beyond the scope of the present manuscript.

II. CANONICAL INTRODUCTION OF SU(2) GAUGE FIELD FOR POLARITON GRAPHENE

Gauge fields appear in the Standard Model of elementary particle interactions via canonical substitution

$$\partial_\mu \to D_\mu = \partial_\mu - iA_\mu, \tag{S7}$$

A_μ can be simple scalar functions of the coordinates in the Minkowsky space, or square matrices of the dimensionality 2 or 3. In the former case one deals with Abelian gauge fields, and in the latter with non-Abelian, or Yang-Mills, gauge fields, for which $[A_\mu; A_\nu] \neq 0$. The necessity of the introduction of the substitution S7 is dictated by the demand to keep the field Lagrangian invariant under the certain class of the transformations, known as gauge transformations.

In non-relativistic quantum mechanics and condensed matter physics synthetic gauge fields can be introduced in the similar way, by imposing the condition of the gauge invariance of the non-relativistic Hamiltonian density of the considered system. Let us show explicitly, how this allows to introduce the SU(2) gauge field for the considered case of the polariton graphene.

Let us start from the case, when TE-TM splitting of the photonic mode can be neglected. The dispersion of the hexagonally patterned microcavity in this case around K and K' points of the Brillouin zone consists of the degenerated pair of the Dirac cones, corresponding to the two orthogonal polarizations. Introducing the wavefunction of a spinor polariton as $\Psi^T = (\Psi_+, \Psi_-)^T$, where $\pm$ signs correspond to polarization degree of freedom, one can write the Hamiltonian density as:

$$\mathcal{H} = \Psi^\dagger \hat{H}_0 \Psi = -i\hbar v_F (\psi_+^*, \psi_-^*) \begin{pmatrix} \tau_z\sigma_x\partial_x + \sigma_y\partial_y & 0 \\ 0 & \tau_z\sigma_x\partial_x + \sigma_y\partial_y \end{pmatrix} \begin{pmatrix} \psi_+ \\ \psi_- \end{pmatrix}. \tag{S8}$$

Note, that as components of the orthogonal polarizations correspond to the individual Dirac dispersions, the functions $\psi_\pm$ are themselves 2-spinors in the pseudospin space corresponding to the upper and lower Dirac cones, where the Pauli operators $\sigma_{x,y}$ act.

This Hamiltonian is invariant under the *global* SU(2) transformation of the type

$$\tilde{\psi} = \omega\psi, \tag{S9}$$

where constant matrix $\hat{\omega}$ belongs to the SU(2) Lie group. This transformation is nothing more but standard rotation in the polarization space. Note, however, that Hamiltonian density S8 is *not* invariant under *local* SU(2) gauge transformation, when the components of the matrix $\hat{\omega} = \hat{\omega}(\mathbf{r})$ depend on the coordinates, as in this case

$$\tilde{\mathcal{H}} = \tilde{\Psi}^\dagger \hat{H}_0 \tilde{\Psi} = \mathcal{H} - i\hbar v_F(\psi_+^*, \psi_-^*)\left(\tau_z\sigma_x \otimes \partial_x\hat{\omega} + \sigma_y \otimes \partial_y\hat{\omega}\right)\begin{pmatrix}\psi_+\\ \psi_-\end{pmatrix} \neq \mathcal{H} \tag{S10}$$

where the sign of direct product $\otimes$ indicates that Pauli matrices $\sigma_{x,y}$ and transformation matrix $\hat{\omega}$ act in different spaces (pseudospin space corresponding to upper and lower Dirac cones and polarization space, respectively). We can, however, restore the invariance, if we make the canonical replacement, performing the substitution S7, where $\mu = x, y$, and 2×2 matrices $i\hat{A}_\mu$ belong to the Lie algebra of SU(2) group (i.e. matrices $A_{x,y}$ themselves are Hermitian) and obey the following gauge transformation:

$$\tilde{\hat{A}}_\mu = \hat{\omega}\hat{A}_\mu\hat{\omega}^{-1} - i\hat{\omega}\partial_\mu\hat{\omega}^{-1}. \tag{S11}$$

The total SU(2) gauge invariant Hamiltonian then reads:

$$\hat{H} = \hbar v_F\left[\tau_z\sigma_x \otimes \left(\hat{q}_x - \hat{A}_x\right) + \sigma_y \otimes \left(\hat{q}_y - \hat{A}_y\right)\right]. \tag{S12}$$

The details of the components of SU(2) gauge potential depend on the choice of the polarization basis, which corresponds to the fixing of the gauge. In particular, in the basis of circular polarizations, the components $\hat{A}_{x,y}$ are given by equations (2) of the main text. Note, that they do not depend on the coordinates, and thus gauge transformation for them coincides with unitary transformation, as it follows from Eq. S11. The Hamiltonian S12 coincides with those given by equation 1 of the main text.

III. ZITTERBEWEGUNG IN POLARITON GRAPHENE

Although the components of the SU(2) gauge field given by equations 2 of the main text are coordinate independent, they have non-trivial impact on the dynamics of the system, including those, corresponding to the spatial variables. This is in striking contrast with the case of a constant Abelian U(1) potential, which can be straightforwardly gauged out by trivial phase transformation. This difference stems from the fact, that components of the field tensor for non-Abelian fields, defined as

$$\hat{F}_{\mu,\nu} = \partial_\mu\hat{A}_\nu - \partial_\nu\hat{A}_\mu + [\hat{A}_\mu; \hat{A}_\nu] \tag{S13}$$

are, due to the presence of the last term, vanishing for Abelian fields, non zero even if $\hat{A}_\mu = const$.

Let us see, how Dresselhaus-type terms affect the spatial dynamics of wavepackets in polariton graphene. We will use Heisenberg representation of the Hamiltonian (1) of the main text

$$\hat{H}^D(t) = \hbar v_F\left[\tau_z\hat{q}_x\hat{\sigma_x}(t) + \hat{q}_y\hat{\sigma_y}(t)\right] + \Delta\left[\tau_z\hat{\sigma_y}(t) \otimes \hat{s}_y(t) - \hat{\sigma}_x(t) \otimes \hat{s}_x(t)\right], \tag{S14}$$

where the operators $\hat{q}_{x,y}$ do not depend on time, as they commute with the Hamiltonian.

Let us consider a wavepacket described by some 4-spinor $\Psi(\mathbf{r})$. The time evolution of the operators of the coordinates is given by the following Heisenberg equations of motion:

$$\frac{d\hat{x}}{dt} = \frac{1}{i\hbar}\left[\hat{x}; \hat{H}^D\right] = v_F\tau_z\hat{\sigma}_x(t), \tag{S15}$$

$$\frac{d\hat{y}}{dt} = \frac{1}{i\hbar}\left[\hat{y}; \hat{H}^D\right] = v_F\hat{\sigma}_y(t), \tag{S16}$$

and the dynamics of the spin operators corresponding to pseudospin and polarization is given by:

$$\frac{d\hat{\sigma}_x}{dt} = \frac{1}{i\hbar}\left[\hat{\sigma}_x; \hat{H}^D\right] = 2v_F\hat{q}_y\hat{\sigma}_z(t) + \frac{2\Delta\tau_z}{\hbar}\hat{s}_y(t)\otimes\hat{\sigma}_z(t), \tag{S17}$$

$$\frac{d\hat{\sigma}_y}{dt} = \frac{1}{i\hbar}\left[\hat{\sigma}_y; \hat{H}^D\right] = -2v_F\tau_z\hat{q}_x\hat{\sigma}_z(t) + \frac{2\Delta}{\hbar}\hat{s}_x(t)\otimes\hat{\sigma}_z(t), \tag{S18}$$

$$\frac{d\hat{\sigma}_z}{dt} = \frac{1}{i\hbar}\left[\hat{\sigma}_z; \hat{H}^D\right] = 2v_F\left[\tau_z\hat{q}_x\hat{\sigma}_y(t) - \hat{q}_y\hat{\sigma}_x(t)\right] - \frac{2\Delta}{\hbar}\left[\tau_z\hat{s}_y(t)\otimes\hat{\sigma}_x(t) + \hat{s}_x(t)\otimes\hat{\sigma}_x(t)\right], \tag{S19}$$

$$\frac{d\hat{s}_x}{dt} = \frac{1}{i\hbar}\left[\hat{s}_x; \hat{H}^D\right] = \frac{2\Delta\tau_z}{\hbar}\hat{\sigma}_y(t)\otimes\hat{s}_z(t), \tag{S20}$$

$$\frac{d\hat{s}_y}{dt} = \frac{1}{i\hbar}\left[\hat{s}_y; \hat{H}^D\right] = \frac{2\Delta}{\hbar}\hat{\sigma}_x(t)\otimes\hat{s}_z(t), \tag{S21}$$

$$\frac{d\hat{s}_z}{dt} = \frac{1}{i\hbar}\left[\hat{\sigma}_z; \hat{H}^D\right] = -\frac{2\Delta}{\hbar}\left[\tau_z\hat{\sigma}_y(t)\otimes\hat{s}_x(t) + \hat{\sigma}_x(t)\otimes\hat{s}_y(t)\right]. \tag{S22}$$

Let us start our analysis from the simplest case $\Delta = 0$. In this regime, the closed set of the linear equations for $\hat{\sigma}_x(t), \hat{\sigma}_y(t), \hat{\sigma}_z(t)$ describes the precession of the pseudospin around an effective magnetic field $\vec{\Omega} = v_F(\tau_z\vec{e}_x + \vec{e}_y)$, and thus allows analytical solution:

$$\hat{\vec{\sigma}}(t) = e^{-i\hat{\Omega}t}\hat{\vec{\sigma}}(0), \tag{S23}$$

where $\hat{\vec{\sigma}}(t) = (\hat{\sigma}_x(t), \hat{\sigma}_y(t), \hat{\sigma}_y(t))^T$, and

$$\hat{\Omega} = 2v_F\begin{pmatrix} 0 & 0 & i\hat{q}_y \\ 0 & 0 & -i\tau_z\hat{q}_x \\ -i\hat{q}_y & i\tau_z\hat{q}_x & 0 \end{pmatrix}. \tag{S24}$$

Consider the particular case of the wavepacket localized around certain value of $\hat{q}_x \approx \langle q_x\rangle$, for which we can put approximately $\hat{q}_y \approx 0$. Choose the initial value of the pseudospin operator as: $\hat{\vec{\sigma}}(0) = (\hat{\sigma}_x(0), 0, \hat{\sigma}_z(0))^T$. Then, according to the equations S23, we get: $\hat{\sigma}_x(t) = \hat{\sigma}_x(0), \hat{\sigma}_y(t) = \hat{\sigma}_z(0)\sin(v_F\tau_z\hat{q}_x t)$, and mean values of x and y coordinated, describing the motion of the center of the wavepacket, can be found as:

$$x(t) = \langle\hat{x}(t)\rangle = x(0) + v_F\tau_z\langle\hat{\sigma}_x(0)\rangle t, \tag{S25}$$

$$y(t) = \langle\hat{y}(t)\rangle = y(0) + v_F\int_0^t\langle\hat{\sigma}_y(t')\rangle dt' = y(0) + v_F\int_0^t\langle\hat{\sigma}_z(0)\sin(v_F\tau_z\hat{q}_x t)\rangle dt' \approx \tag{S26}$$

$$\approx y(0) + \frac{\tau_z\langle\hat{\sigma}_z(0)\rangle}{\langle q_x\rangle}\left[1 - \sin(v_F\tau_z\langle q_x\rangle t)\right].$$

One sees, that the considered wavepacket is steadily displacing along x-axis, but undergoes periodic oscillations along y-axis, which correspond to the well known zitterbewegung effect for relativistic particles.

Now, let us return back to the case where Dresselhaus term is present and $\Delta \neq 0$. In this regime, the Hamiltonian S14 formally corresponds to those of the two interacting spins, placed into external magnetic field acting on only one of them. Clearly, in this case solution for pseudospin operators strongly differs from those, given by Eq. S23, which, according to Eqs. S15,S16 have strong effect on the orbital motion as well.

IV. FURTHER EXPERIMENTAL DETAILS

Here we present further details of the sample and experimental setup. The honeycomb lattice was fabricated from a planar semiconductor microcavity, which was grown on a double-side polished substrate to allow operation in transmission geometry. The sample was patterned to form arrays of overlapping micropillars by etching through the top and bottom DBR stacks (Fig. S3).

The sample was mounted in a continuous-flow cryostat and held at low temperature (< 10 K) for all measurements. For the momentum space images, nonresonant excitation provided by a 637 nm laser was used in a reflection geometry (Fig. S4a). The energy-resolved emission was detected with a 0.75 m spectrometer (1200 gr/mm) and Peltier cooled CCD and recorded in sections by translating the imaging lens. For the real space images, resonant excitation provided by a Ti:sapphire laser was used in a transmission geometry (Fig. S4b). For these measurements the spectrometer grating was set to zero order and the slit opened.

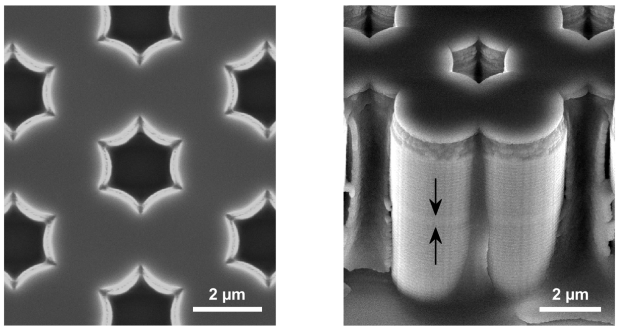

FIG. S3: Left, Overhead view of a honeycomb lattice. Right, Side view showing the top/bottom DBR stacks and cavity layer (shown by black arrows).

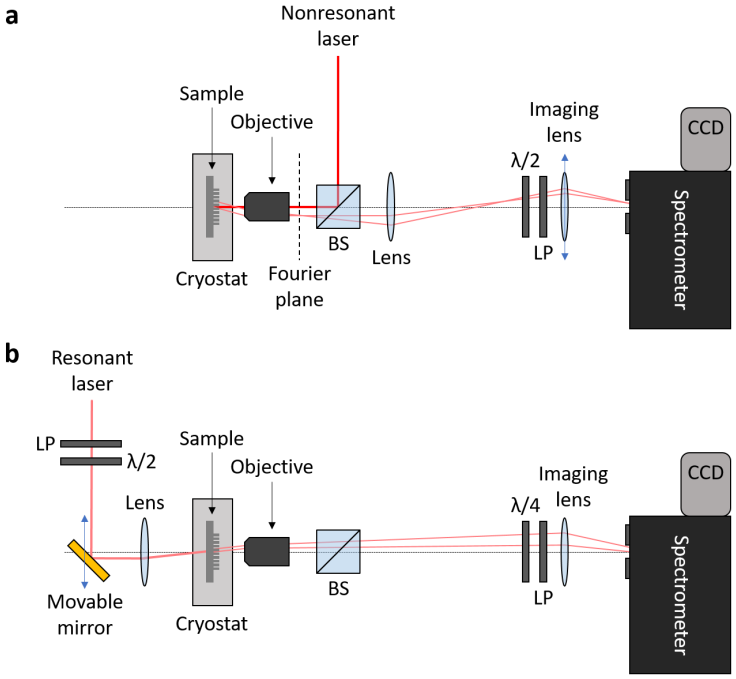

FIG. S4: Schematic diagrams of the reflection (a) and transmission (b) setups.

V. EXPERIMENTAL DETERMINATION OF EFFECTIVE MAGNETIC FIELD TEXTURES

In order to extract the effective magnetic field textures in momentum space, we resolve the emission in horizontal (H), diagonal (D), vertical (V) and anti-diagonal (A) polarizations corresponding to detection angles of 0°, 45°, 90° and 135° respectively. The detection angle, which we denote as α, is defined with respect to the x axis, shown along with the real space orientation of the honeycomb lattice in Fig. S5. Tomographic measurements in the H-V and D-A bases allow us to construct the Stokes parameters $S_1 = (I_H - I_V)/(I_H + I_V)$ and $S_2 = (I_D - I_A)/(I_D + I_A)$ respectively, allowing a complete characterization of the linear polarization state of the emission across momentum space. This is sufficient to determine the effective magnetic field texture since it is entirely in-plane (it has no circular component) in the absence of a real Zeeman field.

In Fig. S6 we show the polarization-resolved momentum space emission in the s bands (corresponding to Fig. 2 of the main text), at the energy of the Γ point at 1.4547 eV (a–d) and the Dirac points at 1.4551 eV (e–h). The total intensity S_0 reveals emission from the centre of the Brillouin zone (BZ) at $k = 0$ in the former case and from the six corners of the BZ forming a hexagon in the latter case. Replicas in the second BZs can also be seen. The

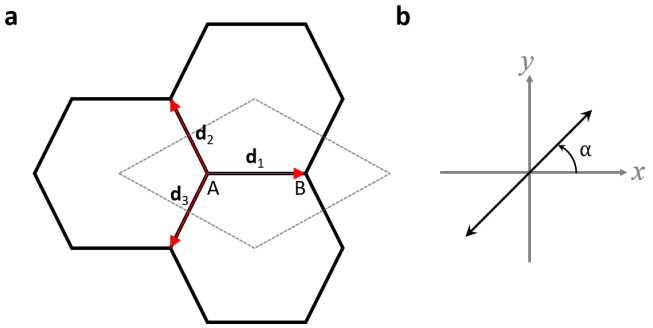

FIG. S5: (a) Real space orientation of the honeycomb lattice, labelled with A and B sublattices and nearest neighbour vectors $\mathbf{d}_1$, $\mathbf{d}_2$ and $\mathbf{d}_3$. The dashed diamond delimits a unit cell. (b) Definition of linear polarization detection angle α.

S_1 and S_2 maps shown allow the linear polarization angle ϕ of the emission to be calculated at each point using $2\phi = \arctan(S_2/S_1)$. Note the factor of two which represents the fact that one only has to rotate a polarization by 180° in real space to return to the same polarization, whilst the Stokes vector has undergone a full 360° rotation.

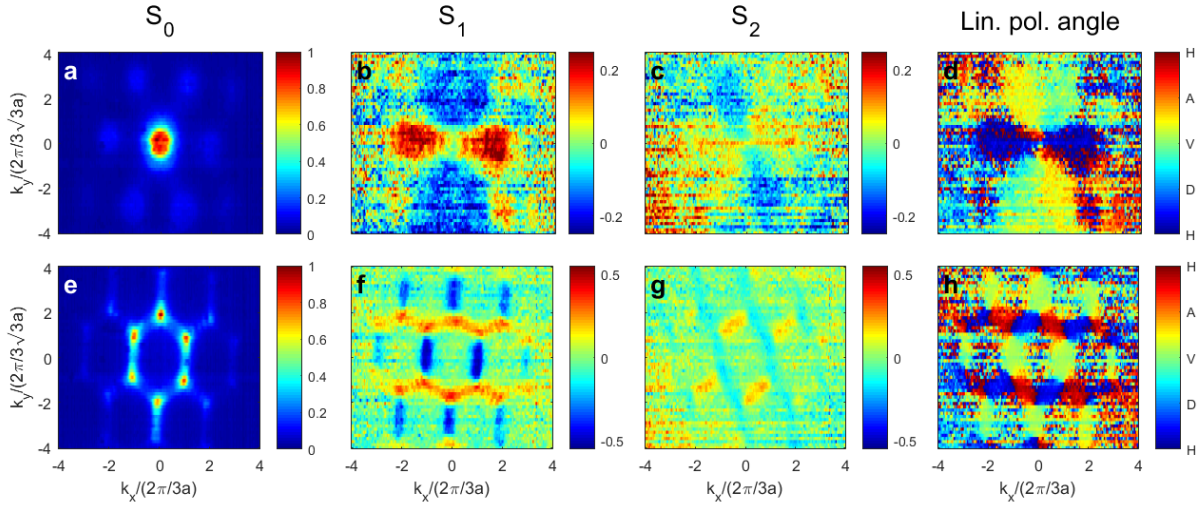

FIG. S6: (a–d) Tomographic images of the momentum space emission at the energy of the Γ point, showing the Stokes parameters S_0 (a), S_1 (b) and S_2 (c), along with the linear polarization angle ϕ (d). (e–h) Tomographic images of the momentum space emission at the energy of the Dirac points, showing the Stokes parameters S_0 (e), S_1 (f) and S_2 (g), along with the linear polarization angle ϕ (h).

In Fig. S7 we show the corresponding momentum space maps for the energy of the Dirac points in the p bands. Since the photoluminescence (PL) intensity is much weaker in the p bands, as can be seen in Fig. S8, the emission is integrated over a small spectral window of ~ 0.2 meV between 1.4581 eV and 1.4583 eV to increase the signal. From the total intensity S_0 we note that the emission pattern is the same as for the energy of the Dirac points in the s bands, with the difference that the brightest points are no longer found at the corners of the first BZ but at the outer corners of the second BZs. This reflects the larger leakage emission intensity (probably of escaping the cavity) for higher k vectors at higher energy. The rectangle in each panel corresponds to the K point for which the linear polarization angle is shown in Fig. 4 of the main text, which is taken from the second BZ due to the higher PL intensity.

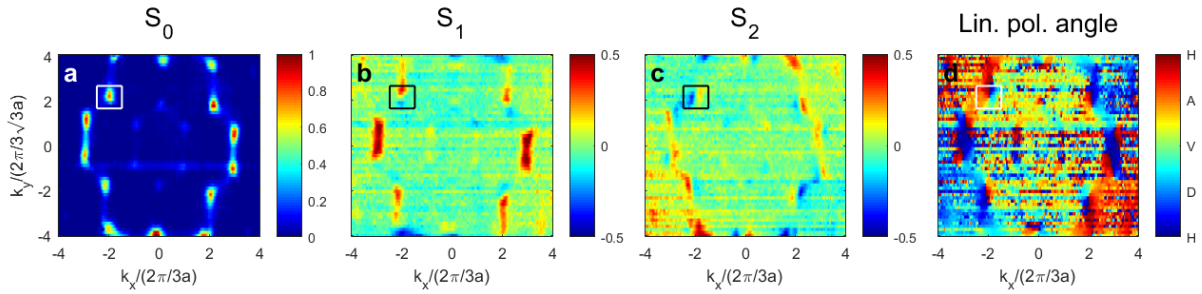

FIG. S7: (a–d) Tomographic images of the momentum space emission at the energy of the Dirac points in the p bands, showing the Stokes parameters S_0 (a), S_1 (b) and S_2 (c), along with the linear polarization angle ϕ (d).

VI. RESONANT EXCITATION MEASUREMENTS

To resonantly excite specific states in the dispersion relation of our honeycomb lattice we control both the energy and incoming angle of the excitation laser. The excitation energy and k vector corresponding to the results shown in Fig. 3 and 4 of the main text are shown in relation to the band structure by black markers in Fig. S8. The three lower energy points correspond to s band excitation [Fig. 3] and the two upper energy points correspond to p band excitation [Fig. 4]. The Γ, K and K' points are excited with angles of 0°, +6.7° and −6.7° respectively.

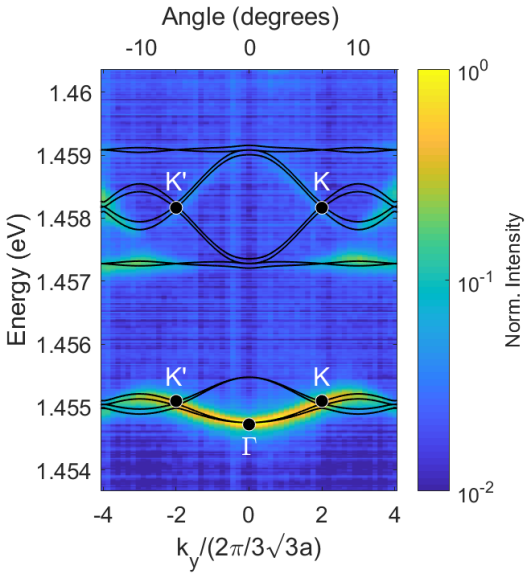

FIG. S8: Dispersion relation measured under low-power non-resonant excitation along $k_x = 0$ ($K' - \Gamma - K$ direction). The black dots show the excitation energy and k vector corresponding to the results shown in Figs. 3 and 4 of the main text. The solid curves show the band structure calculated using the developed tight binding models.

Examples of the real space emission, corresponding to Fig. 3 of the main text (for H polarization) are shown in Fig. S9, which shows the total intensity ($S_0 = I_{\sigma^+} + I_{\sigma^-}$) overlaid with outlines of the experimental structure. The black cross marks the position of the pump spot.

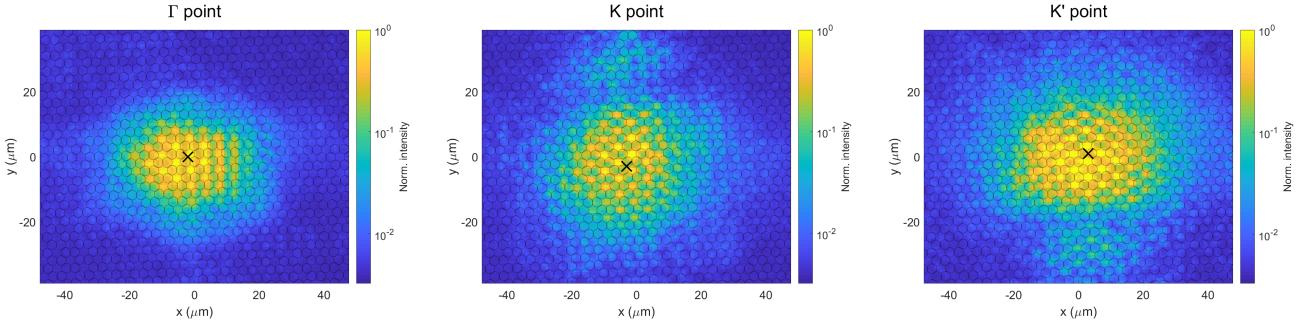

FIG. S9: Measured real space total intensity S_0 under resonant s band excitation for a horizontally polarized pump.

[1] C. Leyder, M. Romanelli, J. Ph Karr, E. Giacobino, T. C. H. Liew, M. M. Glazov, A. V. Kavokin, G. Malpuech, and A. Bramati. Observation of the optical spin hall effect. *Nature Physics*, 3:628, 2007.